Supplement of Atmos. Chem. Phys., 21, 1717–1736, 2021
https://doi.org/10.5194/acp-21-1717-2021-supplement

Atmospheric Chemistry and Physics
Open Access
EGU

Supplement of

Atmospheric-methane source and sink sensitivity analysis using Gaussian process emulation

Angharad C. Stell et al.

Correspondence to: Angharad C. Stell (a.stell@bristol.ac.uk) and Matthew Rigby (matt.rigby@bristol.ac.uk)

1 Loss kinetic isotope effect range

The isotopic fractionation is described by the kinetic isotope effect (KIE), which is defined as

$$\mathrm{KIE} = \frac{k_{12}}{k_{13}}, \tag{1}$$

where k_{12} is the reaction rate constant of $^{12}CH_4$ and k_{13} is the reaction rate constant of $^{13}CH_4$. The KIEs used in MOZART are presented in Table S1. These values are derived from the literature, which are summarised in this section.

The stratospheric loss KIE is calculated by weighting the contribution of Cl and O(^{1}D) to stratospheric methane loss by the ratio given in Saunois et al. (2016), and the soil loss is modelled as negative emissions with isotopic fractionation calculated similarly to Lassey et al. (2007).

Table S1: The one standard deviation range of KIEs examined in the MOZART model.

	Minimum	Maximum	Default value
$^{13C}\mathrm{KIE}_{OH}$	1.0037	1.0041	1.0039
$^{13C}\mathrm{KIE}_{STRAT}$	1.035	1.044	1.0402
$^{13C}\mathrm{KIE}_{Cl}$	1.0635	1.0665	1.065
$^{13C}\mathrm{KIE}_{soil}$	1.0185	1.0235	1.021

1.1 Reaction of CH_4 and OH

The range of literature values for the reaction of CH_4 and OH are presented in Table S2. Rust and Stevens (1980) had experimental difficulties and recorded a large range of values (1.0003 to 1.0078) and Davidson et al. (1987) was superseded by Cantrell et al. (1990). This leaves only Saueressig et al. (2001) and Cantrell et al. (1990). In this work, the two standard deviation range is taken as $^{13C}\mathrm{KIE}_{OH}$=1.0035-1.0043, from the accepted value of Saueressig et al. (2001).

Table S2: Literature values reported for the kinetic isotope effect of CH_4 and OH.

	Reference	KIE	Two standard deviations
Experimental	Saueressig et al. (2001)	1.0039	0.0004
	Cantrell et al. (1990)	1.0054	0.0009
	Davidson et al. (1987)	1.010	0.007
	Rust and Stevens (1980)	1.0036	0.0026
Theoretical	Gupta et al. (1997)	1.010	
	Melissas and Truhlar (1993)	1.005	
	Lasaga and Gibbs (1991)	1.007	

1.2 Reaction of CH_4 and O(^{1}D)

There are very few studies of the KIE of the reaction of CH_4 and O(^{1}D): Saueressig et al. (2001) report a value of 1.013, whereas Davidson et al. (1987) report a value of 1.001 from a single experiment. In this work, we take only the accepted value from Saueressig et al. (2001), which the authors report as having a negligible uncertainty.

1.3 Reaction of CH_4 and Cl

Table S3 shows the literature range of values for $^{13C}\text{KIE}_{Cl}$. There is good agreement between the experimental literature values. The full range of the two standard deviation uncertainty of these experimental studies was taken, to give a range of 1.062 to 1.068.

Table S3: Literature values reported for the kinetic isotope effect of CH_4 and Cl.

	Reference	KIE	Two standard deviations
Experimental	Tyler et al. (2000)	1.0621	0.0001
	Crowley et al. (1999)	1.066	0.002
	Saueressig et al. (1995)	1.066	0.002
Theoretical	Roberto-Neto et al. (1998)	1.06	
	Gupta et al. (1997)	1.034	
	Tanaka et al. (1997)	1.026	

1.4 Loss of CH_4 by soil

The literature values of $^{13C}\text{KIE}_{soil}$ are shown in Table S4. There is good agreement between these studies and so the full range of values are used, giving a two standard deviation range of 1.016 to 1.026.

Table S4: Literature values reported for the kinetic isotope effect of CH_4 and soil.

Reference	KIE	Two standard deviations
Snover and Quay (2000)	1.0173	0.0020
	1.0181	0.0008
Reeburgh et al. (1997)	1.023	
	1.026	
Tyler et al. (1994)	1.022	0.008
King et al. (1989)	1.026	
	1.016	

2 Freshwater emissions dataset

In this work, the Global Lakes and Wetlands Database (GLWD) (Lehner and Döll, 2004) was used to create a global emissions dataset of freshwater bodies. The methane emissions from a freshwater body was weighted according to its percentage of the global freshwater area, to give a global total of 120 $\text{Tg}\,\text{yr}^{-1}$ (Saunois et al., 2016). The Earth was split into three latitude bands: tropical (less than 30° N and S), mid-latitudes (30-50° N and S), and high-latitudes (more than 50° N and S), and weighted according to Saunois et al. (2016) to account for the different climatic conditions: 49 % tropical, 33 % mid-latitudes, and 18 % high-latitudes. The emissions map is time-invariant due to a lack of observational evidence (Natchimuthu et al., 2016; Wik, Thornton, Bastviken, Uhlbäck and Crill, 2016), but it is possible that freshwater emissions have a large seasonal cycle due to the dependency on temperature (Wilkinson et al., 2015). The resulting freshwater emissions distribution can be seen in Fig. S1, and the NetCDF file (along with the code used to create it) is available to be downloaded at https://doi.org/10.17605/OSF.IO/Q9F8P (Stell, 2020).

There are several improvements that could be made to the freshwater emissions dataset. The first is to use a power law to describe the relationship between the freshwater body area and methane emissions (e.g. Bastviken et al., 2004; Wik, Varner, Anthony, MacIntyre and Bastviken, 2016). This relationship means that the many small water bodies missing from GLWD are important (Holgerson and Raymond, 2016), and ideally lakes from the higher resolution GLObal WAter BOdies database (GLOWABO) (Verpoorter et al., 2014) should be included. Additionally, more careful consideration of which bodies to include might be beneficial, for example, the Caspian Sea is somewhat saline and so could be reduced or removed from the map (e.g. Liu and Boone, 1991; Pattnaik et al., 2000). Lake depth is also a key variable in predicting methane emissions from ebullition (Bastviken et al., 2004). Lake depths for the largest lakes are included in Kourzeneva et al. (2012), so there is potential to combine all available databases to extract as much information as possible. Variables such as temperature, water body type, and altitude would also ideally be included. The suggested improvements to the freshwater emission dataset are not required for this work, as the map is latitude-band weighted, so the hemispheric distribution is correct. As this work only uses hemispheric data, this will not majorly impact the results.

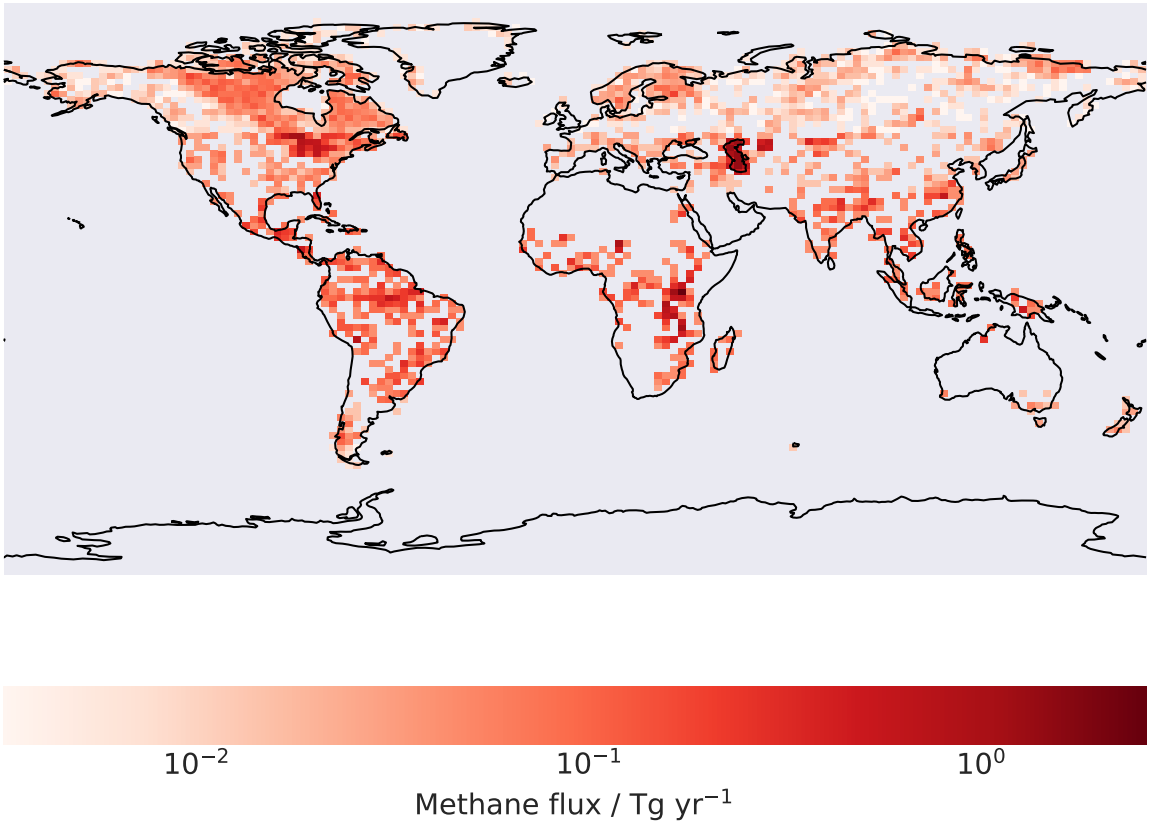

Figure S1: The global distribution of freshwater methane emissions used in this work. Total methane emissions are 120 Tg yr^{-1} (Saunois et al., 2016), which is distributed according to the freshwater area in three latitude bands as described in the text.

3 Emulator Validation

3.1 Relation between emulator errors and inputs

Differences between the emulator prediction and the true model should not correlate with the input values. If correlations are present, this indicates that either some emulator parameters are not optimal or non-stationarity (Bastos and O'Hagan, 2009). In Fig. S2, Fig. S3, Fig. S4, and Fig. S5, the difference between the mean of the prediction for the emulators and the true model value for the validation dataset are plotted against each input parameter value in a separate panel. There is no correlation between any emulator and any input parameter.

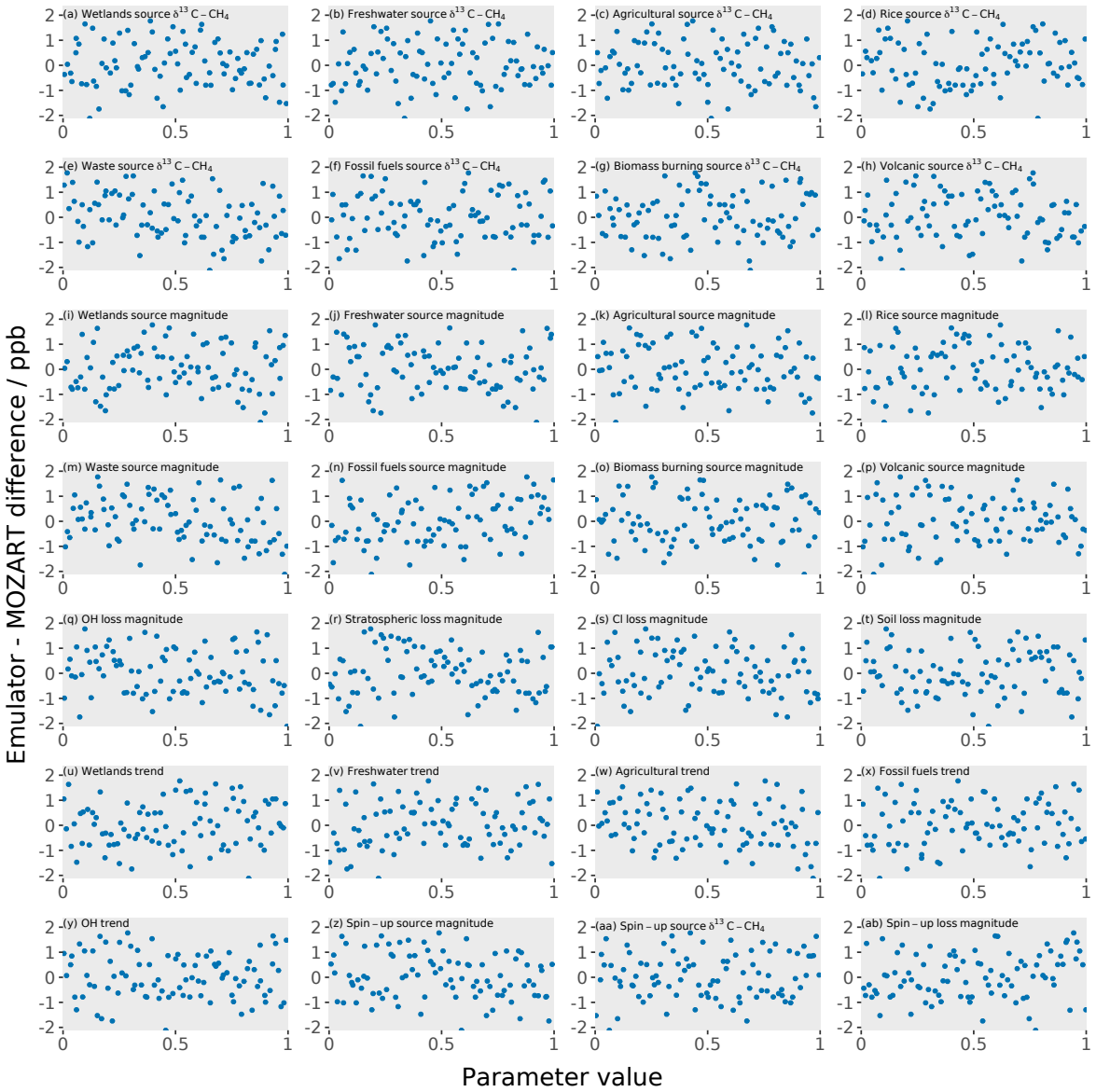

Figure S2: The difference between the Southern Hemisphere mole fraction emulator and the true value in the MOZART model is plotted against each input parameter.

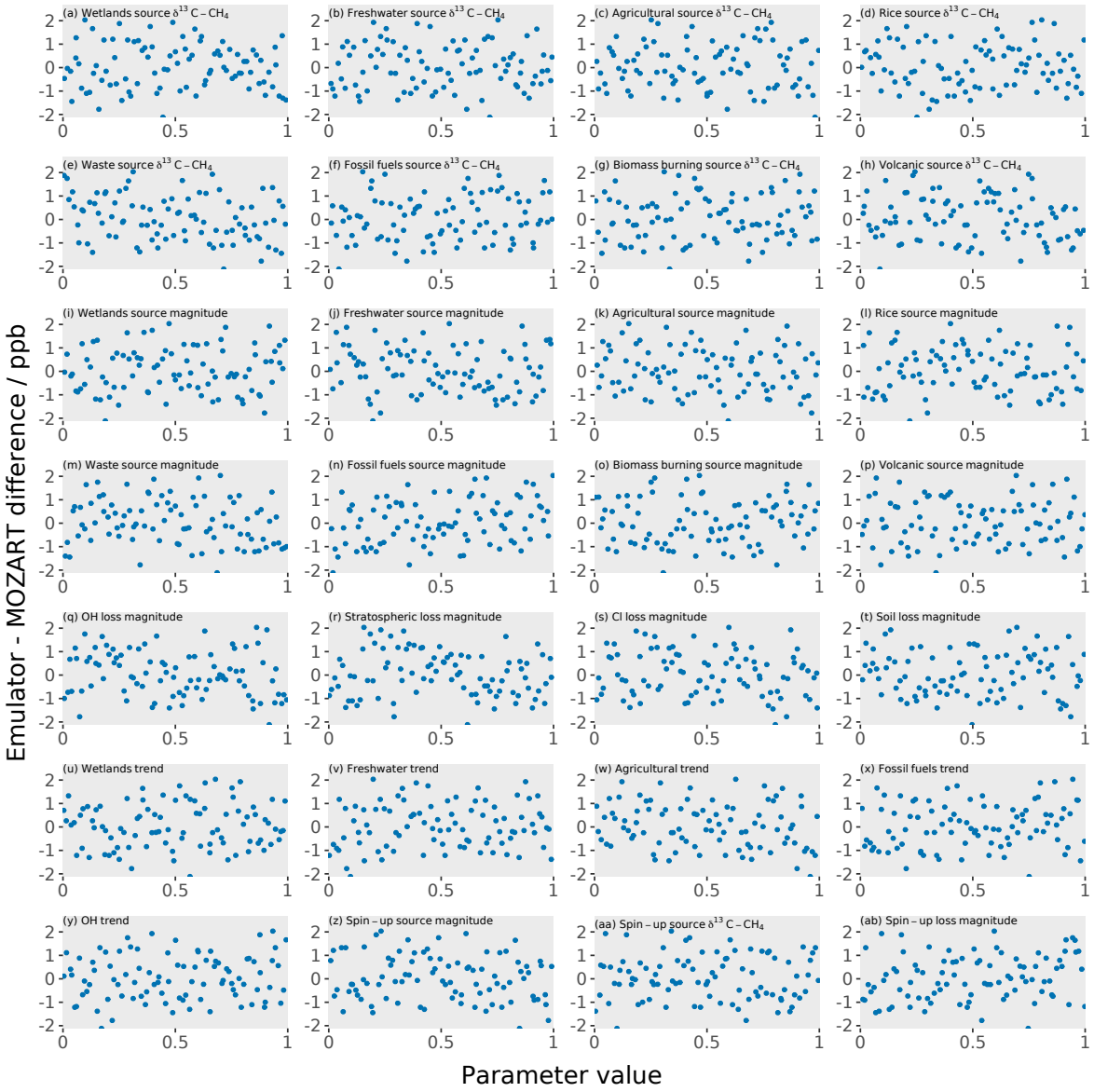

Figure S3: The difference between the Northern Hemisphere mole fraction emulator and the true value in the MOZART model is plotted against each input parameter.

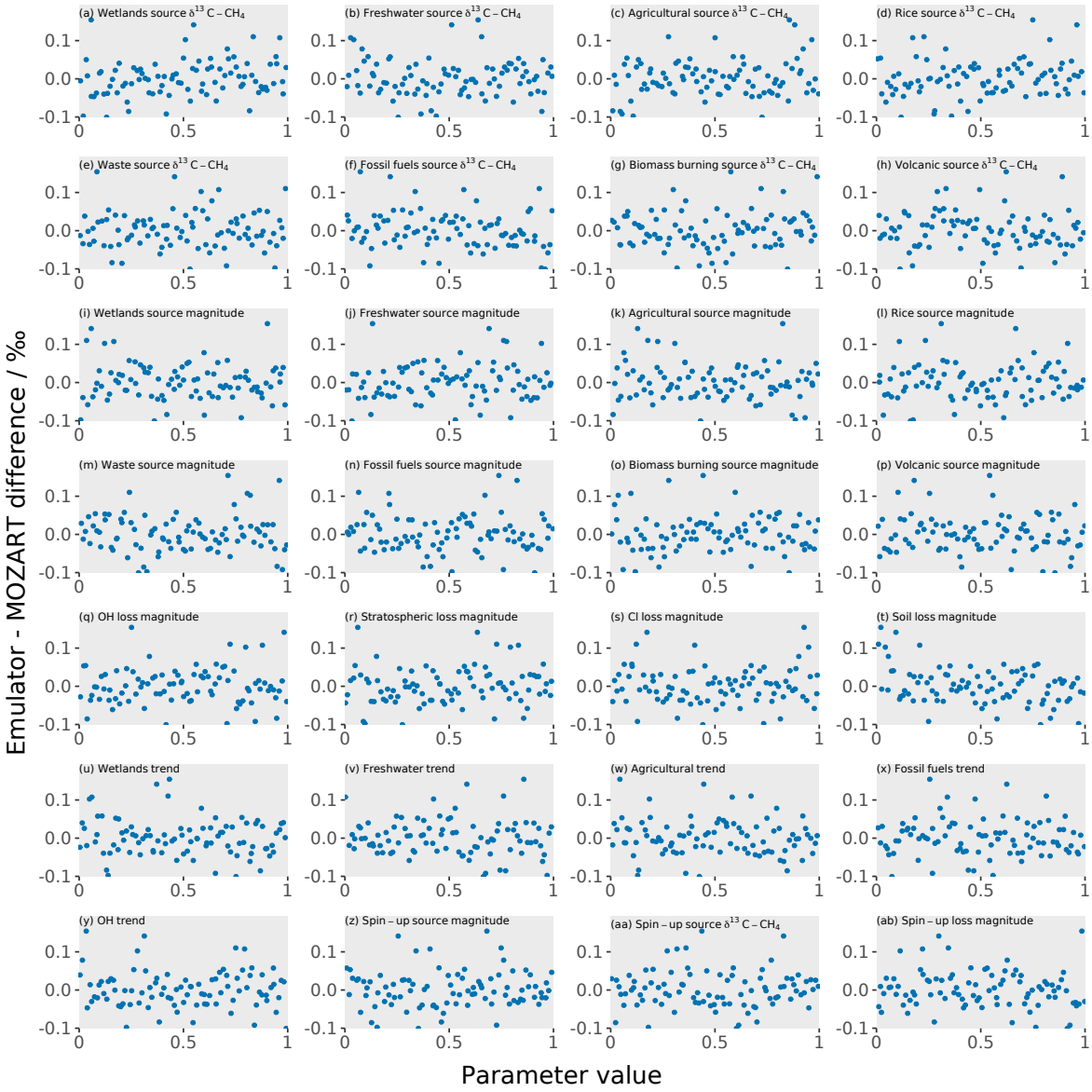

Figure S4: The difference between the Southern Hemisphere δ^{13}C-CH_4 emulator and the true value in the MOZART model is plotted against each input parameter.

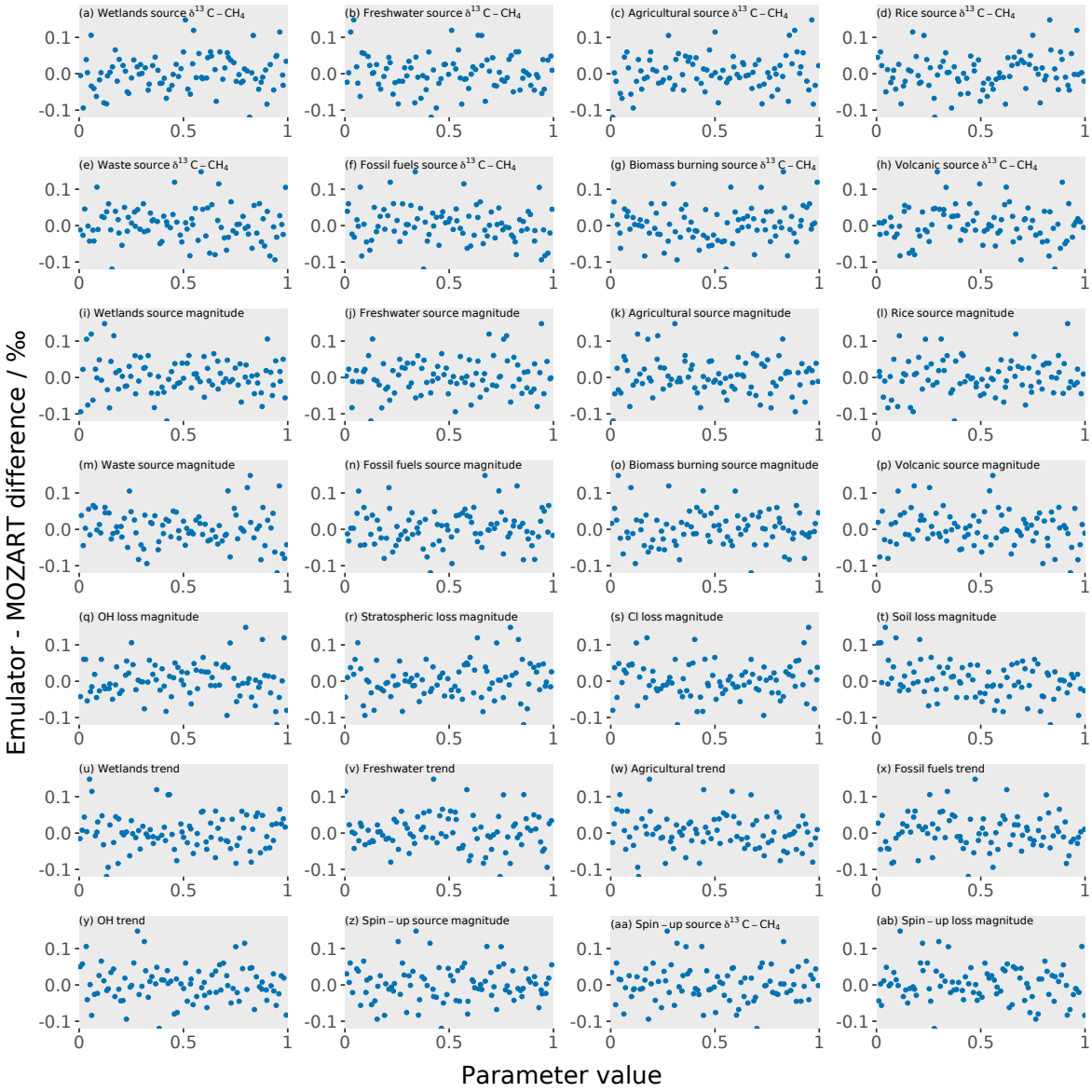

Figure S5: The difference between the Northern Hemisphere δ^{13}C-CH_4 emulator and the true value in the MOZART model is plotted against each input parameter.

3.2 Relation between emulator errors and outputs

Standardised residuals between the emulator and the true model simulation in the validation dataset should also be normally distributed. These residuals are calculated by

$$\epsilon = \frac{y_{em} - y_{mzt}}{\sigma_{em}}, \tag{2}$$

where y_{em} is the emulator prediction for one month, y_{mzt} is the corresponding MOZART output, and σ_{em} is the emulator calculated error for that month. These residuals are compared to a normal distribution in Fig. S6. The residuals are close to normally distributed, with the largest difference for the mole fraction emulators in the middle of the time series. Here the emulator error is larger than that

seen in the residuals. This is because the emulator estimated error is time-invariant (as the emulator error only depends on the difference between the inputs), but the model output range is smaller in the middle of the time series due to the design of the trend parameters. The trend parameters conserve the total magnitude of the source or sink over the time series. Therefore, all the possible trend values have the same magnitude in the centre of the time series, so there is a smaller output range here. This effect is not seen in the δ^{13}C-CH_4 emulators due to the longer time between input changes and δ^{13}C-CH_4 response.

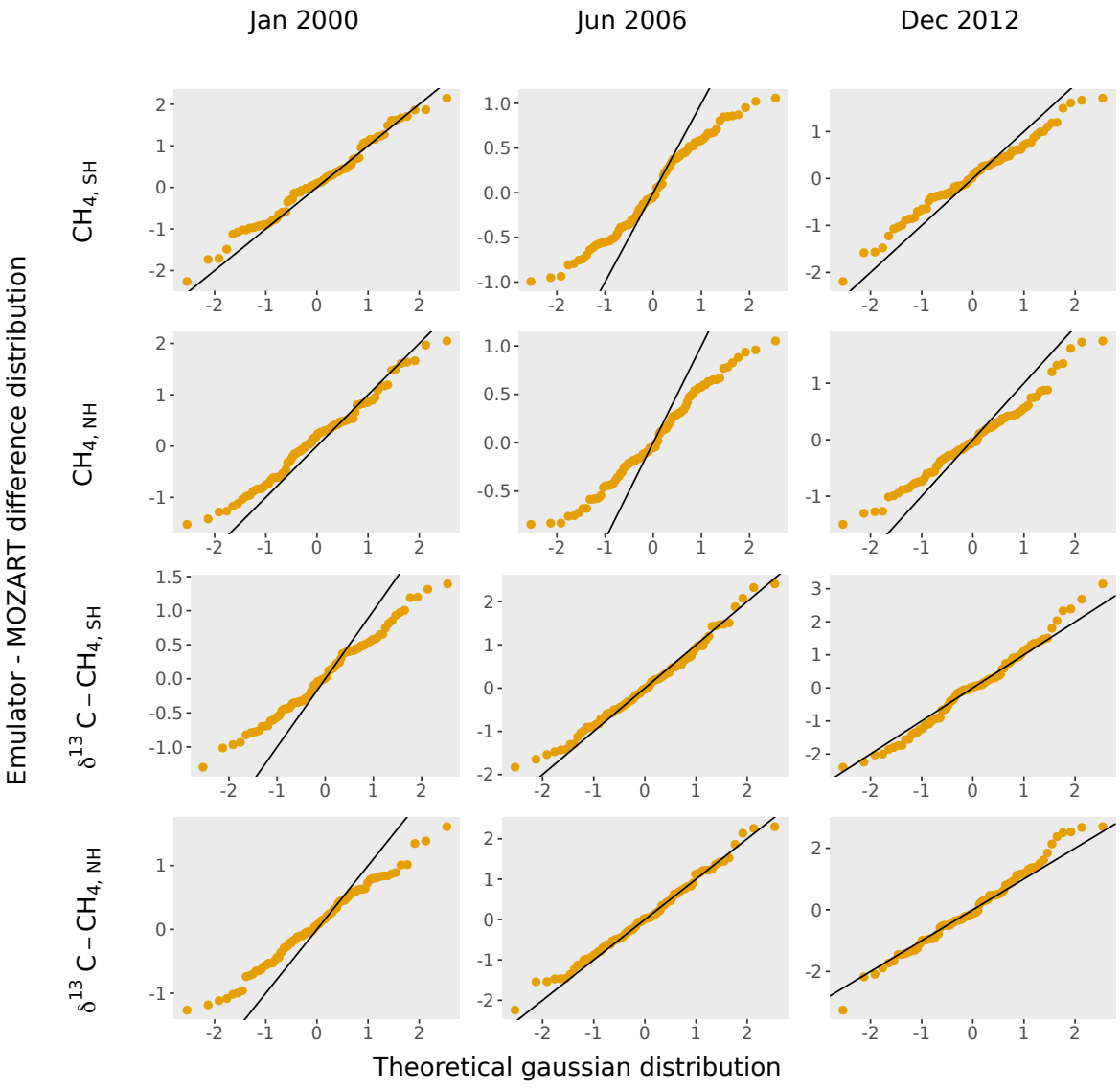

Figure S6: Quantile-quantile plots of the standardised emulator residuals for each hemispheric emulator (each row) at the beginning, middle, and end of the time series (each column). The black line, y=x, is plotted as a visual guide and represents the ideal case that the distribution of the residuals is perfectly Gaussian.

3.3 Auto-correlation functions

Figure S7 shows the mean auto-correlation functions for the MOZART simulations and the emulator predictions. This figure shows that the emulators are able to replicate the MOZART time correlation structure.

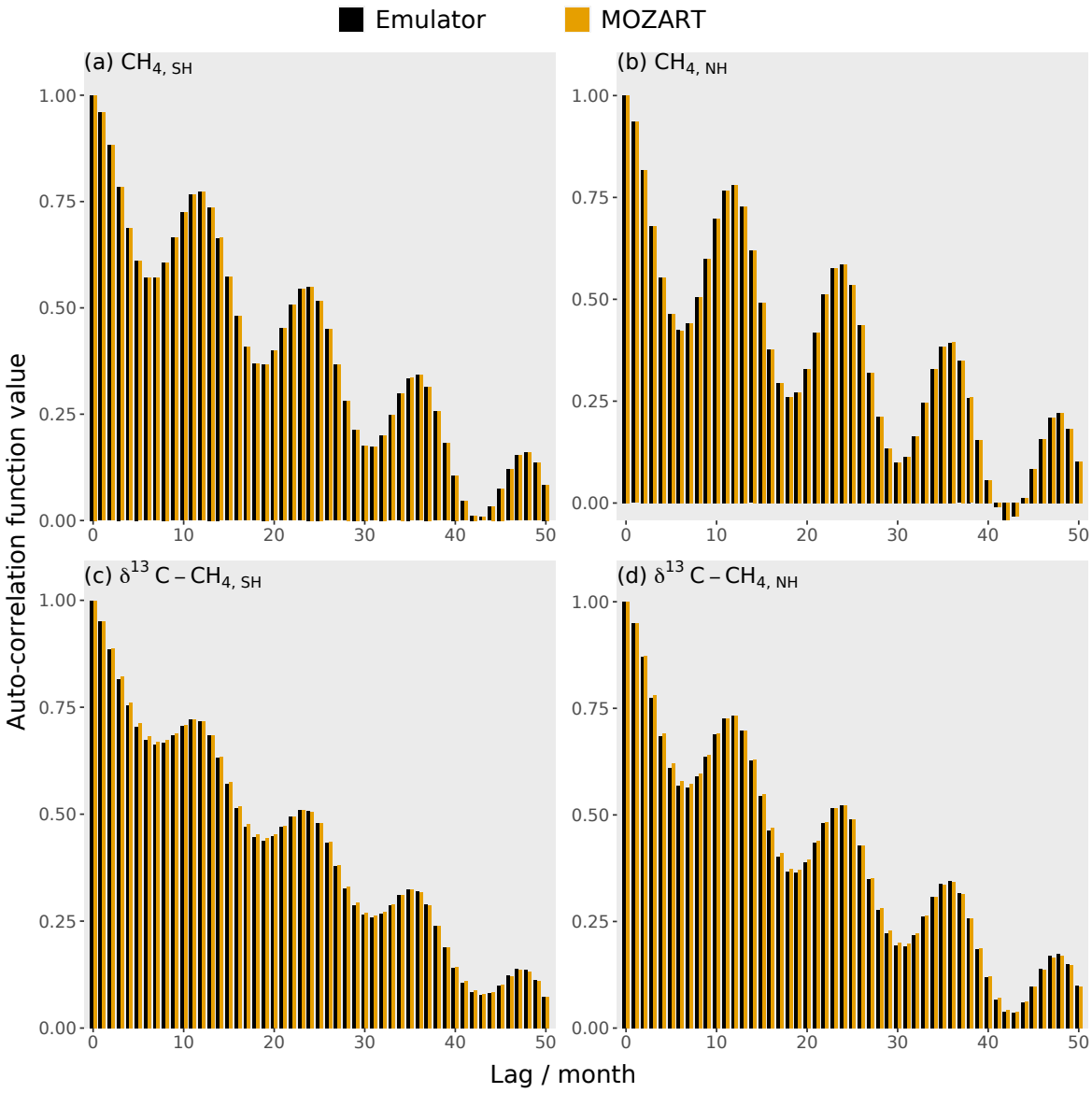

Figure S7: A comparison of the average auto-correlation function: MOZART is shown as the orange bars, and the emulators are shown as the black bars. Each panel shows a different output: (a) the Southern Hemisphere mole fraction, (b) the Northern Hemisphere mole fraction, (c) the Southern Hemisphere δ^{13}C-CH_4, and (d) the Northern Hemisphere δ^{13}C-CH_4.

4 NOAA sites used

Table S5 lists all the station locations, where NOAA (Dlugokencky et al., 1994) and INSTAAR (Miller et al., 2002) take measurements, that were used to construct the MOZART monthly median hemispheric outputs emulated in this work. Only grid cells containing stations measuring the methane mole fraction or δ^{13}C-CH_4 were included in the hemispheric median for the mole fraction or δ^{13}C-CH_4, respectively.

Table S5: All NOAA stations used in this work, along with their latitude, longitude, altitude, and the type of measurement. The units of the altitude data is metres above sea level (masl).

Station	Latitude / ° N	Longitude / ° W	Altitude / masl	Mole fraction	δ^{13}C-CH_4
Alert, Nunavut, Canada	82	297	195		x
Terceira Island, Azores, Portugal	39	333	24	x	
Baring Head Station, New Zealand	-41	175	90	x	
Tudor Hill, Bermuda, UK	32	295	60	x	
Cold Bay, Alaska, USA	55	197	32	x	
Cape Grim, Tasmania, Australia	-41	145	164	x	x
Crozet Island, France	-46	52	202	x	
Easter Island, Chile	-27	251	57	x	
Mariana Islands, Guam	13	145	7	x	
Halley Station, Antarctica, UK	-76	334	35	x	
Storhofdi, Vestmannaeyjar, Iceland	63	340	127	x	
Izana, Tenerife, Canary Islands	28	344	2378	x	
Key Biscayne, Florida, USA	26	280	6	x	
Cape Kumukahi, Hawaii, USA	20	205	9	x	x
Mace Head, County Galway, Ireland	53	350	26	x	x
Sand Island, Midway, USA	28	183	8	x	
Mauna Loa, Hawaii, USA	20	204	3419	x	x
Niwot Ridge, Colorado, USA	40	254	3526		x
Palmer Station, Antarctica, USA	-65	296	15	x	
Ragged Point, Barbados	13	301	20	x	
Shemya Island, Alaska, USA	53	174	28	x	
Tutuila, American Samoa	-14	189	53	x	x
South Pole, Antarctica, USA	-90	335	2817	x	x
Summit, Greenland	73	322	3215	x	
Syowa Station, Antarctica, Japan	-70	40	16	x	
Tae-ahn Peninsula, Republic of Korea	37	126	21		x
Ushuaia, Argentina	-55	292	32	x	
Mt. Waliguan, People's Republic of China	36	101	3815		x
Ny-Alesund, Svalbard, Norway	79	12	479	x	

5 The number of simulations required to build a useful Gaussian process

As a rule of thumb, ten times the number of parameters is a good number of training simulations to train a Gaussian process (e.g. Loeppky et al., 2009). However, this is dependent on the model being emulated and hence the accuracy of emulators trained with different numbers of simulations is tested here. The accuracy of the emulators trained with different numbers of simulations was calculated by leave one out cross validation, where each simulation is removed from the training dataset and the emulator predicts the removed simulation. The residuals between the emulator prediction and the training simulation are combined as the temporal average of the root-mean-square error and are shown in Fig. S8. This figure shows that additional simulations give a diminishing accuracy increase. For many applications, emulators with an error not much smaller than the MOZART invariant parameter error are satisfactory, as the invariant parameter error is an underestimate of the total MOZART error. Therefore, little more than 90 simulations are required.

In general, the number of training simulations required scales linearly with the number of input parameters. However, in a case where a few parameters dominate the output sensitivity, i.e. the

problem is of lower dimensionality than it appears, and the relationship between the inputs and output is close to linear, it is possible to train an accurate emulator with fewer simulations than the linear scaling predicts (O'Hagan, 2006). This is demonstrated in the MOZART emulators, and means that Gaussian process emulation could be possible for many complex atmospheric models with a higher spatial resolution than demonstrated in this work.

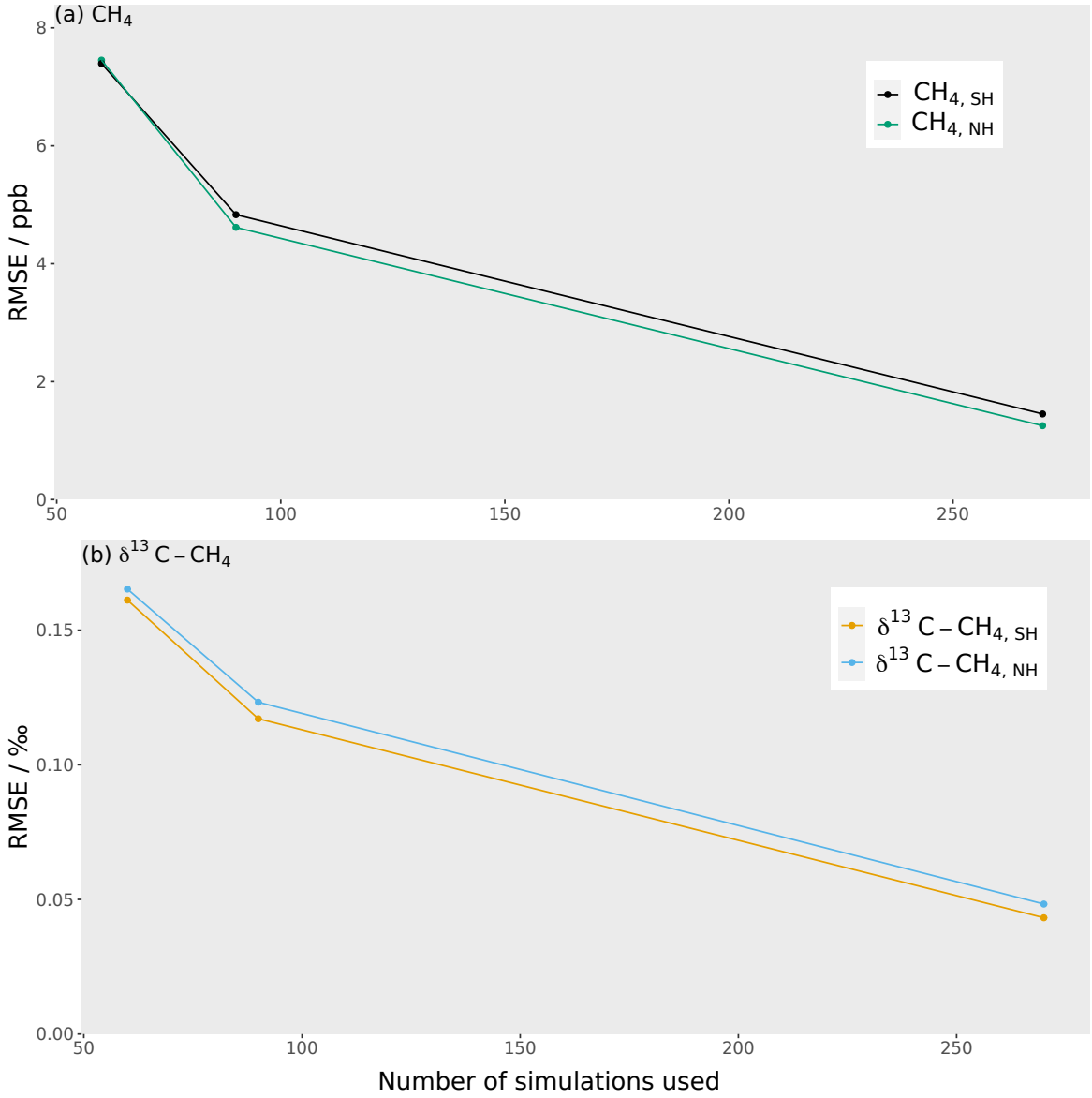

Figure S8: A plot showing how the root-mean-square error (RMSE) between the emulator and MOZART changes for different numbers of training runs in the emulator. Each measurement type is shown in a separate panel: (a) the mole fraction, with the Southern Hemisphere in black and the Northern Hemisphere in green; and (b) δ^{13}C-CH_4, with the Southern Hemisphere in orange and the Northern Hemisphere in blue. There are only three points as each point requires a new Latin hypercube design in order to properly sample the parameter space with a different number of simulations (i.e. an arbitrary sub-set of the largest ensemble cannot be used for this purpose, as it would not be a true Latin hypercube). This means that each point requires a new set of MOZART training simulations, which is computationally expensive to repeat multiple times. However, this function is very unlikely to have multiple minima, and so we think this figure is enough to act as a rough guide.

6 The measurement and model representation uncertainty

The calculation of the combined measurement and model representation uncertainty, from now on referred to as the model-measurement discrepancy uncertainty for brevity, is detailed here. The model-measurement discrepancy uncertainty is calculated by considering four elements that would cause the model output to differ from the observations: the measurement uncertainty, the model representation uncertainty, the different stations sampling in each month of the observations, and the different sample times in the observations. To account for these differences, the standard deviation in 10 000 samples from the uncertainty distributions of these four elements is calculated. The two MOZART simulations in the training dataset closest to the methane mole fraction and δ^{13}C-CH_4 observations were chosen as base simulations, around which these uncertainties are examined.

To account for the measurement uncertainty, a random value drawn from a normal distribution with a mean of zero and the median standard deviation from the NOAA and INSTAAR datasets (1.7 ppb and 0.051 ‰ for the methane mole fraction and δ^{13}C-CH_4, respectively). This random value is added to every 6-hourly output value in each grid cell of the base simulations, in each of the 10 000 samples.

To calculate the horizontal representation uncertainty, a higher spatial resolution (1.89° N × 2.50° W) MOZART simulation with the mean emissions and losses in the training dataset was used. The range of outputs over the high-resolution grid cells within a low-resolution grid cell was calculated. The vertical representation uncertainty is calculated by taking the range of the output in each low-resolution grid cell and the grid cell above and below. For each of the 10 000 samples, a random value drawn from a uniform distribution between minus half the range and plus half the range is added to every 6-hourly output value in each grid cell of the base simulations for both the horizontal and vertical representation uncertainty.

The model hemispheric time series includes all grid cells with measurement stations in every month, regardless of whether there are observations for that station in that month. Therefore, the effect of including different stations in the hemispheric mean is explored by bootstrap resampling. For each of the 10 000 samples, 25 stations for the methane mole fraction and 10 stations for the δ^{13}C-CH_4 (the number of stations included in this study) were chosen by sampling the stations with replacement.

The model hemispheric monthly time series includes all 6-hourly outputs at a station, but the observation hemispheric time series includes only approximately four samples in a monthly mean. To include the effect of having differently timed samples in the monthly output, four random time points are chosen to contribute to each station's monthly value in each of the 10 000 samples.

The hemispheric time series is then calculated, and the standard deviation in the 10 000 samples of the hemispheric time series is used as the model-measurement discrepancy uncertainty. This uncertainty has a median value of 5 ppb and 0.05 ‰ in the Southern Hemisphere, and 10 ppb and 0.08 ‰ in the Northern Hemisphere.

7 The Monte-Carlo calculation of the sensitivity indices

A (N, $2k$) matrix from a Sobol sequence (Sobol', 1967; Antonov and Saleev, 1979) was generated, where N is the number of model simulations (840 000) and k is the number of input parameters (28). This was split into two (N, k) matrices: $\mathbf{A}$ and $\mathbf{B}$. A third matrix $\mathbf{C}_i$, was constructed by replacing the i^{th} column of $\mathbf{B}$ with the i^{th} column of $\mathbf{A}$. The three matrices are input to the emulators to generate

N model outputs each: $\mathbf{y}_A$, $\mathbf{y}_B$, and $\mathbf{y}_{C_i}$. Using these matrices, the first order sensitivity indices can be calculated by

$$S_i = \frac{\frac{1}{N}\sum_{j=1}^{N} \mathbf{y}_A^j \mathbf{y}_{C_i}^j - f_0^2}{\frac{1}{N}\sum_{j=1}^{N} (\mathbf{y}_A^j)^2 - f_0^2}, \tag{3}$$

where

$$f_0^2 = \left(\frac{1}{N} \sum_{j=1}^{N} \mathbf{y}_A^j \right)^2. \tag{4}$$

The total effect indices can be calculated by

$$S_{T_i} = 1 - \frac{\frac{1}{N}\sum_{j=1}^{N} \mathbf{y}_B^j \mathbf{y}_{C_i}^j - f_0^2}{\frac{1}{N}\sum_{j=1}^{N} (\mathbf{y}_A^j)^2 - f_0^2}. \tag{5}$$

As suggested in Saltelli et al. (2000), this work uses both $\mathbf{y}_A$ and $\mathbf{y}_B$ instead of just $\mathbf{y}_A$ to calculate f_0^2 and the denominators in Eq. 3 and Eq. 5 (the variance in the output). This improves the accuracy of f_0^2 and the variance in the output, and hence S_i and S_{T_i}, for a fixed N. Uncertainty in these indices was calculated using bootstrap resampling, with 10 000 resamples.

8 The sensitivity of atmospheric δ^{13}C-CH_4 to the OH loss magnitude

One particular aspect of our sensitivity analysis is somewhat counter-intuitive, and warrants further investigation here; we derive relatively high sensitivity of the δ^{13}C-CH_4 inter-hemispheric difference to a change in global mean OH concentration, but low sensitivity of the global mean δ^{13}C-CH_4 to OH. Here, we investigate the global mean δ^{13}C-CH_4 sensitivity to OH using a box model and the emulator.

The propagation of δ^{13}C-CH_4 signals through the atmosphere can be counter-intuitive and occurs over a long timescale (Tans, 1997). The response of the δ^{13}C-CH_4 global mean to a step change in the global source magnitude, the global source δ^{13}C-CH_4 signature, or the OH concentration is shown in Fig. S9. This figure was generated using the hemispheric box model described in Rigby et al. (2017), and demonstrates the long time needed to reach a steady state, as well as the different responses of the global mean to perturbations in each input. The figure shows that a step-change in the source magnitude or source signature leads to change in δ^{13}C-CH_4 over several decades, with a consistent sign throughout. However, when a step-change in the global OH concentration occurs, the global mean δ^{13}C-CH_4 perturbation exhibits a sign change after around one decade. This sign change occurs because of the competing exchange and fractionation timescales between the different sinks and reservoirs.

A similar experiment to that in Fig. S9 can be conducted with the emulator, starting with a base case with close to constant δ^{13}C-CH_4 and perturbing each parameter independently. The result of this experiment is shown in Fig. S10. Despite the shorter time period investigated, the same pattern as the

box model is seen in the emulator results (note that the emulator does not simulate the model output in the first four years after the perturbation). Of all the non-trend-related inputs, the OH loss magnitude is the only parameter that leads to a transient response with a change of sign. Coincidentally, the point where the sign change occurs is in the middle of the period that we investigated in this paper, thus reducing the sensitivity in the mean over the whole period. Therefore, while there is substantial sensitivity of the global mean δ^{13}C-CH_4 to the global OH concentration during some periods, it happens that the output metric chosen here (the 2000 - 2012 mean) is insensitive to this input. A sign change occurs in both hemispheres (not shown), but at a different rate, so the mean inter-hemispheric difference does not cancel in the same way as the global mean during this period.

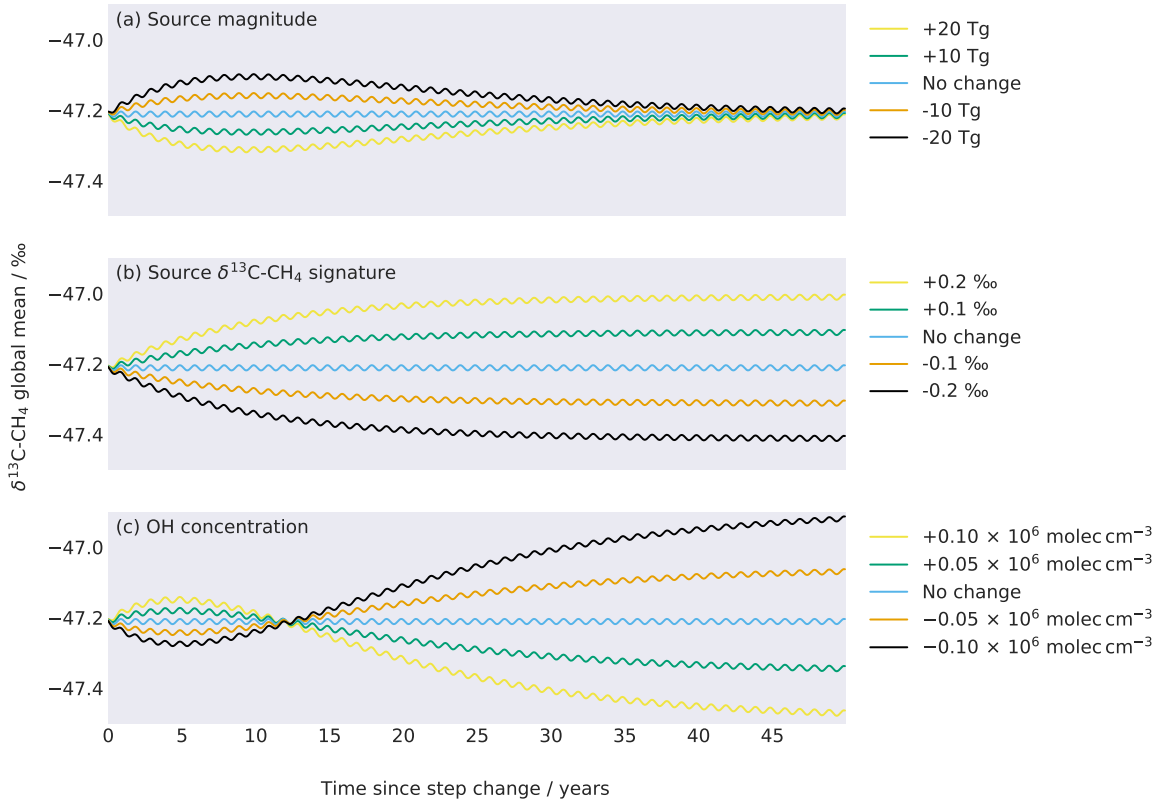

Figure S9: The δ^{13}C-CH_4 global mean following a step change in one of three parameters: (a) the source magnitude, (b) the source δ^{13}C-CH_4 signature, and (c) the OH concentration. Each coloured line represents a different model simulation, labelled in the right hand side legend. This figure was generated using the hemispheric box model described in Rigby et al. (2017).

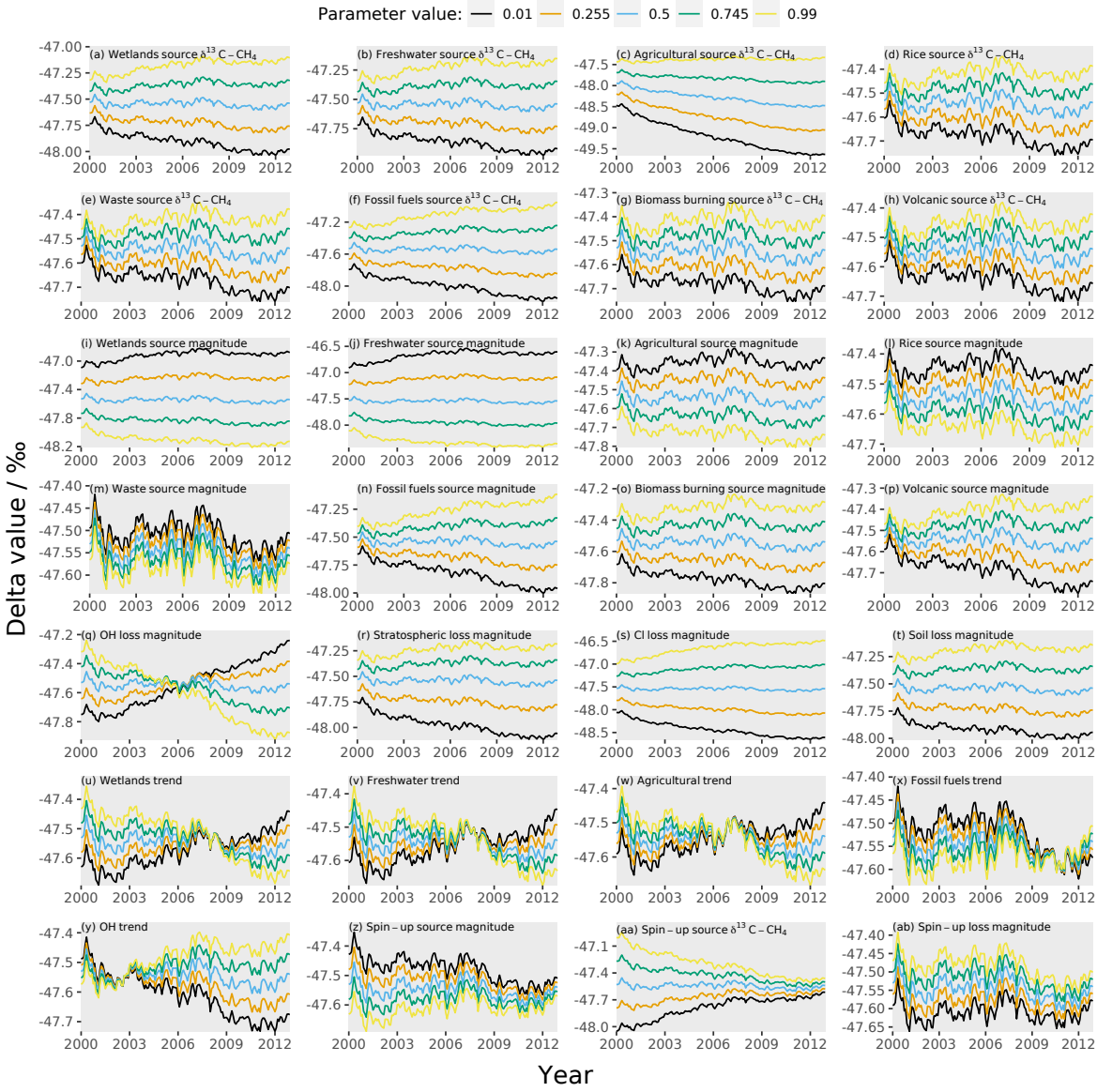

Figure S10: Each subplot shows the emulated δ^{13}C-CH_4 global mean for five different values of the subplot's labelled parameter. The parameters are varied from a base case with approximately constant δ^{13}C-CH_4 over the time period. In this base case, all parameters, apart from the agricultural δ^{13}C-CH_4 signature, take the median parameter value used in this work (a normalised parameter value of 0.5). The agricultural δ^{13}C-CH_4 signature has a normalised parameter value of 0.9 to give an approximately constant δ^{13}C-CH_4 over the time period.

References

Antonov, I. and Saleev, V. (1979), 'An economic method of computing LPτ-sequences', *USSR Computational Mathematics and Mathematical Physics* **19**(1), 243–245. DOI: 10.1016/0041-5553(79)90085-5.

Bastos, L. S. and O'Hagan, A. (2009), 'Diagnostics for gaussian process emulators', *Technometrics* **51**(4), 425–438. DOI: 10.1198/TECH.2009.08019.

Bastviken, D., Cole, J., Pace, M. and Tranvik, L. (2004), 'Methane emissions from lakes: Dependence of lake characteristics, two regional assessments, and a global estimate', *Global Biogeochemical Cycles* **18**(4), GB4009. DOI: 10.1029/2004GB002238.

Cantrell, C. A., Shetter, R. E., McDaniel, A. H., Calvert, J. G., Davidson, J. A., Lowe, D. C., Tyler, S. C., Cicerone, R. J. and Greenberg, J. P. (1990), 'Carbon kinetic isotope effect in the oxidation of methane by the hydroxyl radical', *Journal of Geophysical Research* **95**(D13), 22455–22462. DOI: 10.1029/JD095iD13p22455.

Crowley, J., Saueressig, G., Bergamaschi, P., Fischer, H. and Harris, G. (1999), 'Carbon kinetic isotope effect in the reaction CH4+Cl: a relative rate study using FTIR spectroscopy', *Chemical Physics Letters* **303**(3-4), 268–274. DOI: 10.1016/S0009-2614(99)00243-2.

Davidson, J. A., Cantrell, C. A., Tyler, S. C., Shetter, R. E., Cicerone, R. J. and Calvert, J. G. (1987), 'Carbon kinetic isotope effect in the reaction of CH4 with HO', *Journal of Geophysical Research* **92**(D2), 2195. DOI: 10.1029/jd092id02p02195.

Dlugokencky, E. J., Steele, L. P., Lang, P. M. and Masarie, K. A. (1994), 'The growth rate and distribution of atmospheric methane', *Journal of Geophysical Research* **99**(D8), 17021–17043. DOI: 10.1029/94jd01245.

Gupta, M. L., Mcgrath, M. P., Cicerone, R. J., Rowland, F. S. and Wolfsberg, M. (1997), '12C/13C kinetic isotope effects in the reactions of CH4 with OH and CI', *Geophysical Research Letters* **24**(22), 2761–2764. DOI: 10.1029/97GL02858.

Holgerson, M. A. and Raymond, P. A. (2016), 'Large contribution to inland water CO2 and CH4 emissions from very small ponds', *Nature Geoscience* **9**(3), 222–226. DOI: 10.1038/ngeo2654.

King, S. L., Quay, P. D. and Lansdown, J. M. (1989), 'The 13C/ 12C kinetic isotope effect for soil oxidation of methane at ambient atmospheric concentrations', *Journal of Geophysical Research* **94**(D15), 18273–18277. DOI: 10.1029/JD094iD15p18273.

Kourzeneva, E., Asensio, H., Martin, E. and Faroux, S. (2012), 'Global gridded dataset of lake coverage and lake depth for use in numerical weather prediction and climate modelling', *Tellus, Series A: Dynamic Meteorology and Oceanography* **64**(1), 15640. DOI: 10.3402/tellusa.v64i0.15640.

Lasaga, A. C. and Gibbs, G. V. (1991), 'Ab initio studies of the kinetic isotope effect of the CH4 + OH• atmospheric reaction', *Geophysical Research Letters* **18**(7), 1217–1220. DOI: 10.1029/90GL02679.

Lassey, K. R., Etheridge, D. M., Lowe, D. C., Smith, A. M. and Ferretti, D. F. (2007), 'Centennial evolution of the atmospheric methane budget: What do the carbon isotopes tell us?', *Atmospheric Chemistry and Physics* **7**(8), 2119–2139. DOI: 10.5194/acp-7-2119-2007.

Lehner, B. and Döll, P. (2004), 'Development and validation of a global database of lakes, reservoirs and wetlands', *Journal of Hydrology* **296**(1-4), 1–22. DOI: 10.1016/j.jhydrol.2004.03.028.

Liu, Y. and Boone, D. R. (1991), 'Effects of salinity on methanogenic decomposition', *Bioresource Technology* **35**(3), 271–273. DOI: 10.1016/0960-8524(91)90124-3.

Loeppky, J. L., Sacks, J. and Welch, W. J. (2009), 'Choosing the sample size of a computer experiment: A practical guide', *Technometrics* **51**(4), 366–376. DOI: 10.1198/TECH.2009.08040.

Melissas, V. S. and Truhlar, D. G. (1993), 'Interpolated variational transition state theory and tunneling calculations of the rate constant of the reaction OH+CH4 at 223-2400 K', *The Journal of Chemical Physics* **99**(2), 1013–1027. DOI: 10.1063/1.465401.

Miller, J. B., Mack, K. A., Dissly, R., White, J. W., Dlugokencky, E. J. and Tans, P. P. (2002), 'Development of analytical methods and measurements of 13C/12C in atmospheric CH4 from the NOAA Climate Monitoring and Diagnostics Laboratory Global Air Sampling Network', *Journal of Geophysical Research Atmospheres* **107**(D13), 4178. DOI: 10.1029/2001JD000630.

Natchimuthu, S., Sundgren, I., Gålfalk, M., Klemedtsson, L., Crill, P., Danielsson, Å. and Bastviken, D. (2016), 'Spatio-temporal variability of lake CH 4 fluxes and its influence on annual whole lake emission estimates', *Limnology and Oceanography* **61**(S1), S13–S26. DOI: 10.1002/lno.10222.

O'Hagan, A. (2006), 'Bayesian analysis of computer code outputs: A tutorial', *Reliability Engineering and System Safety* **91**(10-11), 1290–1300. DOI: 10.1016/j.ress.2005.11.025.

Pattnaik, P., Mishra, S. R., Bharati, K., Mohanty, S. R., Sethunathan, N. and Adhya, T. K. (2000), 'Influence of salinity on methanogenesis and associated microflora in tropical rice soils', *Microbiological Research* **155**(3), 215–220. DOI: 10.1016/S0944-5013(00)80035-X.

Reeburgh, W. S., Hirsch, A. I., Sansone, F. J., Popp, B. N. and Rust, T. M. (1997), 'Carbon kinetic isotope effect accompanying microbial oxidation of methane in boreal forest soils', *Geochimica et Cosmochimica Acta* **61**(22), 4761–4767. DOI: 10.1016/S0016-7037(97)00277-9.

Rigby, M., Montzka, S. A., Prinn, R. G., White, J. W. C., Young, D., O'Doherty, S., Lunt, M. F., Ganesan, A. L., Manning, A. J., Simmonds, P. G., Salameh, P. K., Harth, C. M., Mühle, J., Weiss, R. F., Fraser, P. J., Steele, L. P., Krummel, P. B., McCulloch, A. and Park, S. (2017), 'Role of atmospheric oxidation in recent methane growth', *Proceedings of the National Academy of Sciences* **114**(21), 5373–5377. DOI: 10.1073/pnas.1616426114.

Roberto-Neto, O., Coitiño, E. L. and Truhlar, D. G. (1998), 'Dual-level direct dynamics calculations of deuterium and carbon-13 kinetic isotope effects for the reaction Cl + CH4', *Journal of Physical Chemistry A* **102**(24), 4568–4578. DOI: 10.1021/jp980759l.

Rust, F. and Stevens, C. M. (1980), 'Carbon kinetic isotope effect in the oxidation of methane by hydroxyl', *International Journal of Chemical Kinetics* **12**(6), 371–377. DOI: 10.1002/kin.550120602.

Saltelli, A., Ratto, M., Andres, T., Campolongo, F., Cariboni, J., Gatelli, D., Saisana, M. and Tarantola, S. (2000), *Global Sensitivity Analysis: The Primer*, Wiley, Chichester, United Kingdom. DOI: 10.1111/j.1751-5823.2008.00062_17.x.

Saueressig, G., Bergamaschi, P., Crowley, J. N., Fischer, H. and Harris, G. W. (1995), 'Carbon kinetic isotope effect in the reaction of CH4 with Cl atoms', *Geophysical Research Letters* **22**(10), 1225–1228. DOI: 10.1029/95GL00881.

Saueressig, G., Crowley, J. N., Bergamaschi, P., Brühl, C., Brenninkmeijer, C. A. M. and Fischer, H. (2001), 'Carbon 13 and D kinetic isotope effects in the reactions of CH 4 with O(1 D) and OH: New laboratory measurements and their implications for the isotopic composition of stratospheric methane', *Journal of Geophysical Research: Atmospheres* **106**(D19), 23127–23138. DOI: 10.1029/2000JD000120.

Saunois, M., Bousquet, P., Poulter, B., Peregon, A., Ciais, P., Canadell, J. G., Dlugokencky, E. J., Etiope, G., Bastviken, D., Houweling, S., Janssens-Maenhout, G., Tubiello, F. N., Castaldi, S., Jackson, R. B., Alexe, M., Arora, V. K., Beerling, D. J., Bergamaschi, P., Blake, D. R., Brailsford, G., Brovkin, V., Bruhwiler, L., Crevoisier, C., Crill, P., Covey, K., Curry, C., Frankenberg, C., Gedney, N., Höglund-Isaksson, L., Ishizawa, M., Ito, A., Joos, F., Kim, H. S., Kleinen, T., Krummel, P., Lamarque, J. F., Langenfelds, R., Locatelli, R., Machida, T., Maksyutov, S., McDonald, K. C., Marshall, J., Melton, J. R., Morino, I., Naik, V., O'Doherty, S., Parmentier, F. J. W., Patra, P. K., Peng, C., Peng, S., Peters, G. P., Pison, I., Prigent, C., Prinn, R., Ramonet, M., Riley, W. J., Saito, M., Santini, M., Schroeder, R., Simpson, I. J., Spahni, R., Steele, P., Takizawa, A., Thornton, B. F.,

Tian, H., Tohjima, Y., Viovy, N., Voulgarakis, A., Van Weele, M., Van Der Werf, G. R., Weiss, R., Wiedinmyer, C., Wilton, D. J., Wiltshire, A., Worthy, D., Wunch, D., Xu, X., Yoshida, Y., Zhang, B., Zhang, Z. and Zhu, Q. (2016), 'The global methane budget 2000-2012', *Earth System Science Data* **8**(2), 697–751. DOI: 10.5194/essd-8-697-2016.

Snover, A. K. and Quay, P. D. (2000), 'Hydrogen and carbon kinetic isotope effects during soil uptake of atmospheric methane', *Global Biogeochemical Cycles* **14**(1), 25–39. DOI: 10.1029/1999GB900089.

Sobol', I. (1967), 'On the distribution of points in a cube and the approximate evaluation of integrals', *USSR Computational Mathematics and Mathematical Physics* **7**(4), 86–112. DOI: 10.1016/0041-5553(67)90144-9.

Stell, A. C. (2020), 'Global methane freshwater emission map for atmospheric modelling'. DOI: 10.17605/OSF.IO/Q9F8P.
URL: *https://osf.io/q9f8p/*

Tanaka, N., Xiao, Y., Hatakeyama, S. and Ueda, S. (1997), Determination of carbon KIE of CH4 + CI reaction: Large reaction chamber experiment and its implications to atmospheric methane chemistry, *in* 'EOS Trans. Amer. Geophys. Union, 78, Sprint Meeting Suppl., S75'.

Tans, P. P. (1997), 'A note on isotopic ratios and the global atmospheric methane budget', *Global Biogeochemical Cycles* **11**(1), 77–81. DOI: 10.1029/96GB03940.

Tyler, S. C., Ajie, H. O., Rice, A. L. and Cicerone, R. J. (2000), 'Experimentally determined kinetic isotope effects in the reaction of CH4 with Cl: Implications for atmospheric CH4', *Geophysical Research Letters* **27**(12), 1715–1718. DOI: 10.1029/1999GL011168.

Tyler, S. C., Crill, P. M. and Brailsford, G. W. (1994), '13C/12C Fractionation of methane during oxidation in a temperate forested soil', *Geochimica et Cosmochimica Acta* **58**(6), 1625–1633. DOI: 10.1016/0016-7037(94)90564-9.

Verpoorter, C., Kutser, T., Seekell, D. A. and Tranvik, L. J. (2014), 'A global inventory of lakes based on high-resolution satellite imagery', *Geophysical Research Letters* **41**(18), 6396–6402. DOI: 10.1002/2014GL060641.

Wik, M., Thornton, B. F., Bastviken, D., Uhlbäck, J. and Crill, P. M. (2016), 'Biased sampling of methane release from northern lakes: A problem for extrapolation', *Geophysical Research Letters* **43**(3), 1256–1262. DOI: 10.1002/2015GL066501.

Wik, M., Varner, R. K., Anthony, K. W., MacIntyre, S. and Bastviken, D. (2016), 'Climate-sensitive northern lakes and ponds are critical components of methane release', *Nature Geoscience* **9**(2), 99–105. DOI: 10.1038/ngeo2578.

Wilkinson, J., Maeck, A., Alshboul, Z. and Lorke, A. (2015), 'Continuous Seasonal River Ebullition Measurements Linked to Sediment Methane Formation', *Environmental Science & Technology* **49**(22), 13121–13129. DOI: 10.1021/acs.est.5b01525.